Acta Materialia 203 (2021) 116456

Contents lists available at ScienceDirect

Acta Materialia

journal homepage: www.elsevier.com/locate/actamat

Interstitial carbon induced FCC-Ti exhibiting ultrahigh strength in a $Ti_{37}Nb_{28}Mo_{28}$-C_7 complex concentrated alloy

Shan Jiang[a], Lujun Huang[a,b,*], Xiang Gao[c], Gang Liu[d], Rui Zhang[a], Yang Jiao[a], Shang Peng[c], Qi An[a], Shuai Wang[a], Lin Geng[a,b]

[a] School of Materials Science and Engineering, Harbin Institute of Technology, P.O. Box 433, Harbin 150001, PR China
[b] State Key Laboratory of Advanced Welding and Joining, Harbin Institute of Technology, Harbin 150001, PR China
[c] Center for High Pressure Science &Technology Advanced Research, Haidian District, Beijing, 100094, P.R. China
[d] State Key Laboratory for Mechanical Behavior of Materials, Xi'an Jiaotong University, Xi'an, 710049, China

ARTICLE INFO

Article history:
Received 4 June 2020
Revised 22 October 2020
Accepted 30 October 2020
Available online 9 November 2020

Keywords:
FCC-Ti
complex concentrated alloy
Cs-corrected STEM
micropillar compression
DFT

ABSTRACT

An interstitial carbon induced-FCC-Ti was observed in a carbon-doped $Ti_{37}Nb_{28}Mo_{28}$-C_7 (atomic percentage) complex concentrated alloys (TNMC alloys). Not only the true crystal structure of this FCC-Ti was directly characterized using Cs-corrected STEM, but also the mechanical properties were tested by nanoindentation and micro-pillar compression for the first time. The FCC-Ti exhibited a high nano hardness of 17.8 GPa and a high elastic modulus of 233.1 GPa. The micropillar compression tests demonstrated the ultrahigh strengths of the interstitial C induced FCC-Ti (4.48 GPa at [1 1 1] direction, 2.67 GPa at [1 0 1] direction, and a CRSS of 1.12 ± 0.07 GPa). The nature of this FCC allotropic transformation was determined to be a rearrangement of lattice structure caused by interstitial C atoms, based on *ab-initio* studies. Findings in this study provide insights into the characteristics of FCC-Ti as well as the role of interstitial atoms in RCCAs which could open up unlimited possibilities in future material designing.

1. Introduction

As a class of promising engineering material, titanium materials, such as titanium alloys, titanium matrix composites, and Ti-Al intermetallics, have attracted increasing attention over the past century owing to the low density, high strength, and superior corrosion resistance [1–6]. Ti also plays a critical role in emerging and rising refractory complex concentrated alloys (RCCAs) [7–10] intended for high-temperature applications to fabricate the Ti-rich RCCAs [11–14] to cope with the high-density problem brought by concentrated heavy alloying elements [15]. However, with less heavy refractory elements used, the strength enhancement would also drastically decrease. In recent years, doping non-metallic interstitial atoms (e.g., boron, carbon, and oxygen) was found with the ability to effectively strengthen the 3d transition metal CCAs (Co-Cr-Fe-Mn-Ni CCAs) without much sacrifice of ductility [16–19]. The impact of different interstitial elements on the 3d transition metal CCAs can be various, such as dislocation pinning, tuning stability of metastable matrix, grain boundary decorating, and forming reinforcing phases. Considering the low atomic mass of interstitial elements, applying the "interstitial CCAs" concept instead of using heavy metallic elements, could effectively alleviate the critical high-density problem. Yet, the application of this novel alloying strategy in RCCAs is quite rare [9,20], despite its tremendous potential. Thus, to further utilize this novel alloying strategy, it is of great significance to continue exploiting in the interstitial RCCAs compositional space and figure out the role of interstitial atoms in RCCAs. Here, based on the high-temperature application background, a carbon-doped $Ti_{37}Nb_{28}Mo_{28}$-C_7 RCCA (TNMC alloy) with relatively lower density was designed and fabricated, and due to the doped C atoms, an unexpected face-centered cubic phase of Ti (FCC-Ti) was formed in the body-centered cubic RCCA. In fact, titanium exhibits multiple allotropic phases under different conditions. Namely, hexagonal close-packed (HCP) phase (α-Ti), body-centered cubic (BCC) phase (β-Ti), hexagonal ω-phase, α' and orthorhombic α'' martensitic phases [21–27]. The discovery of FCC-Ti dates back to the year of 1969 when Wawner and Lawless [28] revealed such a structure within an epitaxial grown Ti nanofilm. The FCC-Ti has been found in different material systems and across multiple length scales: Nanosized FCC-Ti was found in epitaxial grown Ti nanofilm [29–35], interfaces between α-phase and β-phase in α+β titanium alloys [36–39], cp-Ti powder [40], Ti-Al powders after severe plastic deformation [41], and a metastable β-type alloy [42]. Recently, sub-micro scale FCC-Ti was observed

* Corresponding author.
E-mail address: huanglujun@hit.edu.cn (L. Huang).

https://doi.org/10.1016/j.actamat.2020.10.075
1359-6454/

in deformed Ti (~300nm) [43–46], in-situ heated Nb-Ti-Si alloy (50~500nm) [47], sintered Ti-Mo-Fe alloy (500~1200nm) [48], Ti–20Zr–6.5Al–4V alloy (weight percentage) aged at high temperatures [49], FIB fabricated TEM samples [50] and in-situ heated Ti-O TEM sample (~400nm) [51]. The nature of the HCP to FCC allotropic transformation of titanium was also discussed: the formation of nano-sized FCC-Ti is due to the energy minimization and it was reported that the nano FCC-Ti could be stable in a large temperature range within the critical size (~27 nm at 882 °C, and 5-7 nm at room temperature) [52,53]; the formation of the sub-microsized FCC-Ti, on the other hand, is achieved by the sequential gliding of a/3 <1 $\bar{1}$ 0 0>-type Schockley partials along every other {0 0 0 1} plane of the HCP lattice. According to these studies, the lattice constants of the FCC-Ti were inconsistent and varied from 4.02 Å [54] to 4.40 Å [30]. However, as the research on the FCC-Ti accumulated, some of the reported FCC-Ti was eventually proved to be artifacts induced during sample preparation. According to systematic researches on the α-β interface phase in Ti alloys by D. Banerjee et al. [55–58], the FCC interface phase was determined to be titanium hydrides formed during TEM sample preparation. The same conclusion has also been found to be true in the cold-rolled cp-Ti TEM samples, that the so called "deformation induced FCC-Ti" has a great chance to only be titanium hydride artifact [59]. The cause of such a artefacts could be ascribed to the hydrogen absorption during the electropolishing process which could be easily overlooked [60]. And the difficulties in characterizing hydrogen element make it even harder to detect such an artifact. Therefore, it is critical to carefully and thoroughly examine the FCC phase of titanium to rule out any possibility for it being titanium hydrides, oxides, carbides, and nitrides artifacts. Even though FCC-Ti has been studied systemically for half a century, yet this novel allotropic phase of Ti still cannot be utilized for the phase transformation mechanism and mechanical properties of the FCC-Ti are still lacking.

In order to have a better understanding of this hidden allotropic phase of Ti and the effect of interstitial C atoms in this RCCAs, a systematic investigation was carried out on this novel FCC-Ti. Microstructure and crystallographic structures of the interstitial carbon induced FCC-Ti were carefully examined and determined using transmission electron microscopy (TEM) and state-of-the-art double Cs-corrected scanning transmission electron microscopy (STEM). Especially, the crystal structure was determined by direct observation of the true atomic arrangement for the first time. The nature of this FCC-Ti allotropic transformation was revealed by ab-initio calculations. The FCC-Ti was found to possess high hardness and modulus according to the nanoindentation test. The micropillar compression tests on the single crystal FCC-Ti of different orientations provided the mechanical properties at a micro-scale which could rule out the size effect of mechanical tests. Findings in this work provide critical insights into not only the characteristics of FCC-Ti but also the role of interstitial atoms in RCCAs and could open up unlimited possibilities in future material designing.

2. Experimental

2.1. Alloy synthesis

The TNMC alloy was fabricated by powder metallurgy method using high purity spherical titanium powder with a mean diameter of 100 μm, angular niobium and molybdenum powder with a mean diameter of 5 μm as starting materials. 1 wt.% stearic acid was used as carbon source and possess controlling agent. The powders were ball milled at 300 rpm for 10 hrs with a ball-to-powder weight ratio of 20:1 in a high purity argon atmosphere. Stainless steel vails with stainless steel balls were used as milling medium. Then the ball-milled powders were filled in a graphite die and hot-pressing sintered at 1300 °C for 1.5 h with a 40 MPa uniaxial pressure applied. The sintering process was carried out in a vacuum of 10^{-2} Pa. To avoid the reaction between the powder and graphite, a thin layer of boron nitride (BN) was sprayed on the inner surface of the die and the punches.

2.2. Microstructure characterizations and sample preparation

X-ray diffraction (XRD) characterization of the mixed powders and the as-sintered alloy were carried out on a Panalytical Empyrean X-ray diffractometer with Cu K-α radiation. The phase distribution and the grain sizes were characterized by electron back-scattered diffraction (EBSD) on a Zeiss SUPRA 55 scanning electron microscope (SEM), the EBSD sample was prepared by the ion etching method. The overall chemical composition of the alloy was determined by glow-discharge optical emission spectroscopy (GDOES) on a LECO GDS850A spectrometer. Element distribution of the alloy and chemical composition quantification of each phase were characterized on a JEOL JXA-8230 electron probe microanalyzer (EMPA) equipped with a wavelength dispersive X-ray spectrometer (WDS). TEM diffraction contrast imaging, energy-dispersive X-ray spectroscopy (EDS) mapping, and selected area electron diffraction (SAED) were carried out on an FEI TALOS F200X TEM equipped with Super-X EDS system with an accelerating voltage of 200 kV. The diffraction contrast images were taken using the Φ 30 μm objective aperture, and the SAED was carried out using the Φ 10 μm selective area aperture which is suitable for performing SAED on grains larger than 100 nm. STEM imaging and electron energy-loss spectroscopy (EELS) analysis were performed using an aberration-corrected JEOL ARM200F microscope. The STEM microscope was operated at 200 kV, using a convergence angle of 30 mrad, and inner/outer angles of about 78/200 mrad and 12/25 mrad for atomic resolution HAADF and ABF imaging, respectively. The TEM and STEM specimen were prepared by mechanical grinding and followed ion milling (GATAN PIPS II MODEL 695) and were plasma cleaned right before inserting into the microscope. To minimize the influence of contamination build-up induced by the electron beam, atomic resolution STEM imaging, and EELS characterization were all taken at different positions. Micropillars of the FCC-Ti with different orientations were fabricated by focused ion beam (FIB) technique according to the EBSD IPF mapping on an FEI Helios NanoLab 600i DualBeam SEM using the top-down method. The micropillars were final-milled down to a diameter of 3 μm to 5 μm and a length-diameter ratio larger than 3:1 with a beam current of 80 pA.

2.3. Mechanical properties tests

Nanoindentation tests were carried out on an Agilent G200 Nano Indenter with a Berkovich diamond tip, at least five indentations on each phase were carried out to ensure reliability. Micropillar compression tested were carried out on a Hysitron TI950 Nanomechanical Test Instrument using a flat diamond punch with a diameter of Φ20 μm. The compression strain rate was controlled to be 8×10^{-4} s^{-1}. The compressive engineering stress and strain were calculated using the area of the cross-section at mid-height and the height of the pillar.

2.4. Ab-initio studies

The cohesive energies and generalized stacking fault energy curves were calculated on the Cambridge Sequential Total Energy Package (CASTEP) code based on density functional theory

(DFT), and the generalized gradient approximation (GGA) in the Perdew, Becke and Ernzerhof (PBE) form [33]. For the cohesive energy calculations and geometry optimization were performed using the Broyden–Fletcher–Goldfarb–Shanno (BFGS) minimizer until the system reached the convergence criteria: total energy tolerance of 10^{-5} eV/atom, maximum force tolerance of 0.03 eV/Å, maximum stress tolerance of 0.05 GPa, and maximum displacement tolerance of 0.001 Å. The 8 × 8 ×8 Monkhorst Pack k-point grids and an energy cutoff of 400 eV were set.

For the generalized stacking fault energy (GSFE) curves calculations, the cutoff energy was set to be 400 eV and the k-points grids were set as 5 × 8 ×1 Monkhorst Pack grids. The supercells were created from the geometry optimized unit cell of the FCC-Ti, which consisted of 12 layers of (1 1 1) planes (x: [1 $\bar{1}$ 0], y: [1 $\bar{1}$ 2], and z: [1 1 1]) with the stacking sequence of ABCABCABCABC. A 15 Å – thick vacuum region was set at z-direction to avoid the influence caused by the periodic boundary condition. The GSFE was calculated by rigid shearing method along the [1 $\bar{1}$ 2] direction. The top 4 layers were incrementally displaced along the [1 $\bar{1}$ 2] direction at a step size of $\frac{a/\sqrt{6}}{10}$ Å, while the bottom 8 layers were fixed to mimic the bulk material. After a displacement of $\frac{a}{\sqrt{6}}$ Å, the stacking sequence was deformed as ABCABCABABCA with an intrinsic stacking fault structure. The GSFE value of the supercell with a displacement of n($\frac{a}{\sqrt{6}}$) Å was then calculated according to the following equation.

$$\gamma_{GSF}^{n} = \frac{E_{SF}^{n} - E_0}{A}$$

Where E_{SF}^{n} is the total energy of the supercell after displacement of n($\frac{a}{\sqrt{6}}$) Å and E_0 is the total energy of the perfect lattice, A denotes the area of the fault plane, γ_{GSF}^{n} is the GSFE value at a displacement of n($\frac{a}{\sqrt{6}}$) Å.

The polycrystalline bulk modulus and shear modulus were calculated using the Voigt-Reuss-Hill average estimation (K_{VRH} and G_{VRH}) based on the stiffness matrix (elastic tensor C_{ij} and compliance tensor s_{ij}) from the DFT calculation results according to the equations below [61,62]:

$$9K_{VRH} = 9K_V = 9K_R = (C_{11}+C_{22}+C_{33}) + 2(C_{12}+C_{23}+C_{31})$$

$$2G_{VRH} = G_V + G_R$$

where G_V and G_R are given by:

$$15G_V = (C_{11}+C_{22}+C_{33}) - (C_{12}+C_{23}+C_{31}) + 3(C_{44}+C_{55}+C_{66})$$

$$15/G_R = (s_{11}+s_{22}+s_{33}) - (s_{12}+s_{23}+s_{31}) + 3(s_{44}+s_{55}+s_{66})$$

the Young's modulus (E) was calculated according to the relation

$$E = 3K(1-2\upsilon)$$

where υ, the isotropic Poisson ratio, is calculated by

$$\upsilon = 3(K_{VRH} - 2G_{VRH})/(6K_{VRH} + 2G_{VRH})$$

3. Results and Discussion

3.1. Microstructure characterizations of the TNMC alloy

The SEM secondary electron image of the as-sintered TNMC alloy is shown in Fig. 1**a**, indicating a two-phase microstructure: a matrix phase (light grey phase) and an irregular shaped second phase (dark grey) surrounded by the matrix phase. Fig. 1**b** shows the XRD pattern evolution of the fabrication process of the TNMC alloy. After a 10-hour ball milling, mechanical alloying and phase transformation have taken place in the mixed elemental powders, that the diffraction peaks of HCP structured α-Ti phase can no longer be detected and a new set of diffraction peaks of a BCC phase was observed. As shown in Fig. 1**b**, the diffraction peaks of the alloying elements disappeared and left only one BCC structured solid solution phase and one FCC structured phase in the as-sintered alloy. Base on Bragg's equation, the lattice parameters of the BCC and FCC phases were determined to be 3.20 Å and 4.22 Å, respectively. The chemical composition of the TNMC alloy was determined to be $Ti_{39.1}Nb_{27.2}Mo_{27.4}C_{6.3}$ (atomic percentage) by the GDOES, which is close to the designed chemical composition of the TNMC complex concentrated alloy. As shown in Fig. 1**e-j**, the EPMA-WDS mappings, two phases with distinct element content can be observed: one contains Ti and C (denoted as Ti-C phase) with the average C concentration of 26.6±1.6 at.%, the other one contains Ti, Nb, and Mo (denoted as (Ti, Nb, Mo) phase), with an average chemical concentration of $Ti_{28.4}Nb_{36.2}Mo_{35.4}$. Oxygen impurity could also be detected in the TNMC alloy. according to the EPMA-WDS quantification, the oxygen content in the Ti-C phase is slightly higher than that in the (Ti,Nb,Mo) phase, which are 1.1±0.21 wt.% (2.6±0.49 at.%) and 0.4±0.042 wt.% (1.9±0.21 at.%), respectively. Compared with the EBSD inverse pole figure (IPF) map and the EBSD phase map (Fig. 1**c**), the Ti-C phase showed an anisometric polycrystal morphology with an average grain size of approximately 30 μm which is similar to the typical grain morphology of the α+β Ti alloys, while the (Ti,Nb,Mo) phase exhibited a relatively uniaxial grain morphology. Based on the EBSD characterization, the phase fraction of the Ti-C phase and the (Ti,Nb,Mo)-phase are 21.45% and 78.55%, respectively.

3.2. Characterization of the FCC-Ti

To determine the crystal structure of the Ti-C phase and the (Ti,Nb,Mo) phase, SAED of the two phases were taken according to the TEM-EDS mapping (grain A and grain B marked in Fig. 2, respectively) indicating that the (Ti,Nb,Mo)-phase is of BCC crystal structure. Interestingly, the Ti-C phase exhibited an unexpected FCC crystal symmetry while the concentration of C suggests that it was too low for titanium carbides, given the C concentration of titanium carbides ranges from 38 at.% to 50 at.%, according to the equilibrium Ti-C phase diagram [63]. The FCC crystal symmetry of the Ti-C phase was further confirmed by a serial of SAED patterns taken along different zone axes and tilting angles (see Supplementary Fig. S1). The acquired patterns match perfectly with the Kikuchi map of an FCC lattice simulated using PTClab software [64]. According to Fig. S2 in the supplementary material, the Ti-C phase and the (Ti,Nb,Mo)-phase exhibited a typical Kurdjumov-Sachs orientation relationship [65], which are <1 1 0>FCC//<1 1 1>BCC, {1 1 1}FCC//{1 1 0}BCC. As has been well documented in the literature that the titanium carbide with a NaCl-type crystal structure [66] shows similar SAED patterns with the FCC lattice. Thus, the possibility of titanium carbides could not be excluded only by conventional TEM studies.

Aberration-corrected STEM was carried out to examine the atom configuration of the FCC Ti-C phase. Fig. 3**a-d** shows the high angle annular dark-field (HAADF) image and corresponding annular bright-field (ABF) image that simultaneously taken from the Ti-C phase. Fig. 3**a-d** show the STEM-HAADF image with atomic number contrast [67–70] alongside with the ABF image displays an absorptive contrast and can detect both light (including C) and heavy atoms [71–73]. According to the atomic resolution STEM images, the atomic columns in the Ti-C phase were arranged as an FCC structure projected along [1 1 0] direction. Most of the atomic columns show a uniform contrast, and the lattice constant measured directly from the atomic resolution images is 4.20 Å which is in good consistency with that measured by XRD, therefore we can conclude that no extra C atomic columns occupied the 0.5,

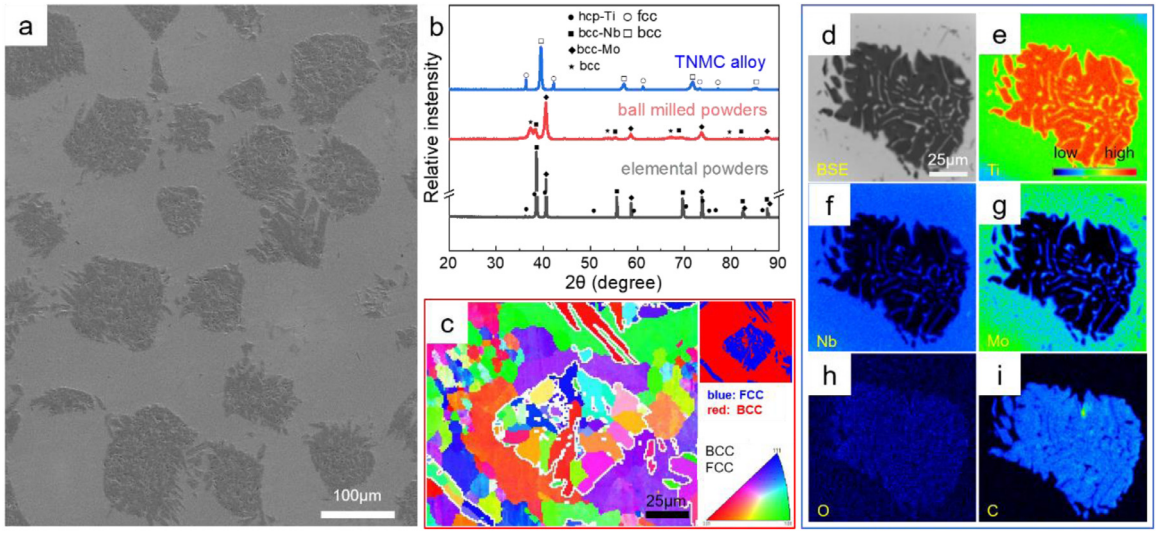

Fig. 1. a SEM secondary electron image showing the microstructure of the as-sintered TNMC alloys; b XRD patterns of the Ti, Nb, Mo elemental powder, the ball-milled powder, and the as-sintered TNMC alloy; c EBSD IPF map showing the grain morphology of the TNMC alloy (the white thick line shows the phase boundary) with the inset showing the distribution of the BCC phase and the FCC phase; d-i SEM backscattered electron image and EMPA WDS mappings of Ti, Nb, Mo, O, and C.

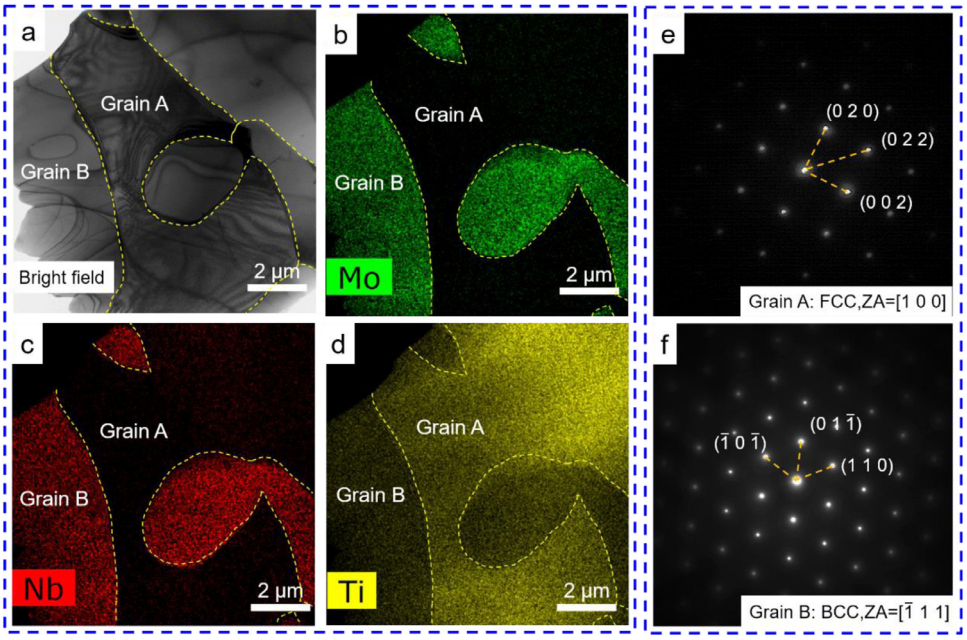

Fig. 2. TEM characterization of the TNMC alloys: a bright field image; b-d EDS-mapping of Mo, Nb, and Ti; e and f SAED patterns taken from different phases according to the EDS mapping.

0.5, 0.5 positions of the face-centered lattice to form an ordered sub-stoichiometry δ-Ti$_x$C [74,75]. It should be mentioned that faint contrast of the atomic columns could be observed at the interstitial sites of the FCC lattice (see Fig. S3 in the supplementary material), indicating the existence of short-range ordering (SRO) in the FCC-Ti-C phase.

Furthermore, EELS was performed to identify the elements' chemical states in the Ti-C phase. As shown in Fig. 3**g**, the electron energy loss near edge structure (ELNES) of the C-*K* edge consists of two energy loss peaks (1s→$\pi*$ transition peak at 285 eV and 1s→$\sigma*$ transition peak at 294 eV) which is similar to that of the amorphous carbon. The intensity of the $\pi*$ edge is much lower than the $\sigma*$ edge, from which we can deduce that no strong bonding between the C atoms and Ti atoms as in the titanium carbides. The ELNES of Ti-$L_{2,3}$ edge is shown in Fig. 3**h**, the ELNES contains 2 sharp edges caused by the 2p → 3d transition: Ti-L_3 at 456 eV and Ti-L_2 at 462 eV. Comparing to the standard profiles and reported results [76,77], we believe that the C and Ti atoms in the Ti-C phase were all at zero valence state and no chemical shifts were detected indicating no ionic bonds were formed in the Ti-C phase [78]. As demonstrated by Chen and Kamran [79], the bonds in the titanium carbides exhibit a dominantly ionic character which would cause a change of the ELNES. Therefore, from the valence state point of view, it can be concluded that the FCC phase we found in the TNMC alloy is indeed an FCC-Ti solid solution phase with interstitial C atoms dissolved into the lattice (denoted as FCC-Ti-C phase) instead of a C deficient δ-Ti$_x$C phase. While the (Ti, Nb, Mo)-phase showed a substitutional solid solution BCC structure with the Ti, Nb, and Mo atoms distributed randomly in the BCC lattice.

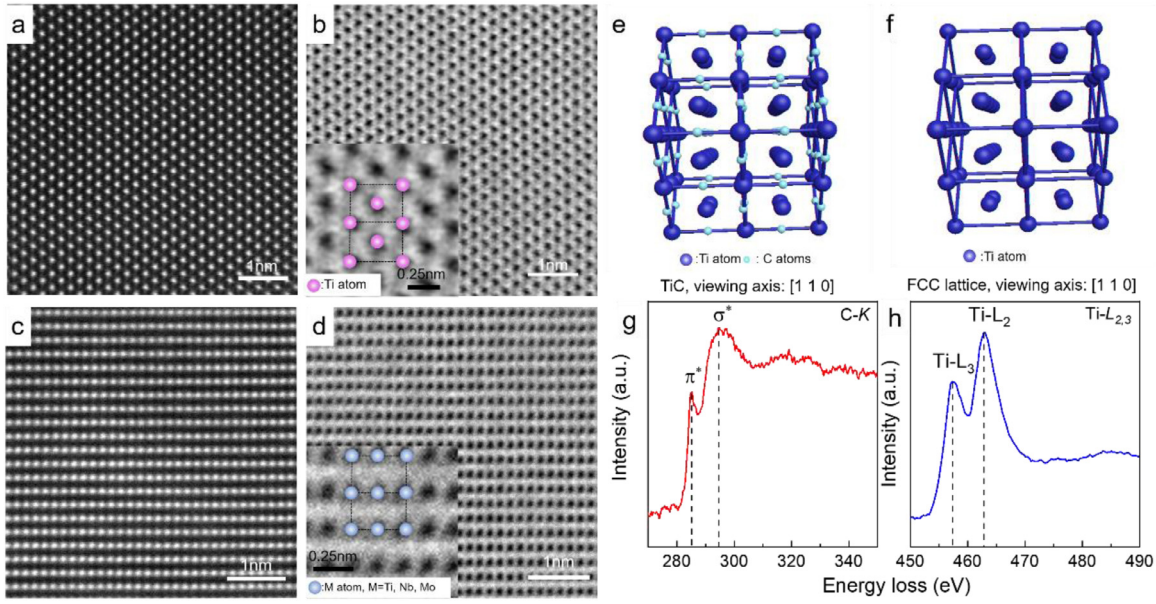

Fig. 3. STEM imaging and EELS characterization of the TNMC alloys: a and b atomic-resolution HAADF and ABF images of the Ti-C phase along its [1 1 0] zone axis; c and d atomic-resolution HAADF and ABF images of the (Ti,Nb,Mo)-phase along its [1 1 0] zone axis; e and f Schematics of TiC with the NaCl-type structure and FCC-Ti with the FCC structure; g and h ELNES spectra of the C *K* and Ti *L* edges of the Ti-C phase.

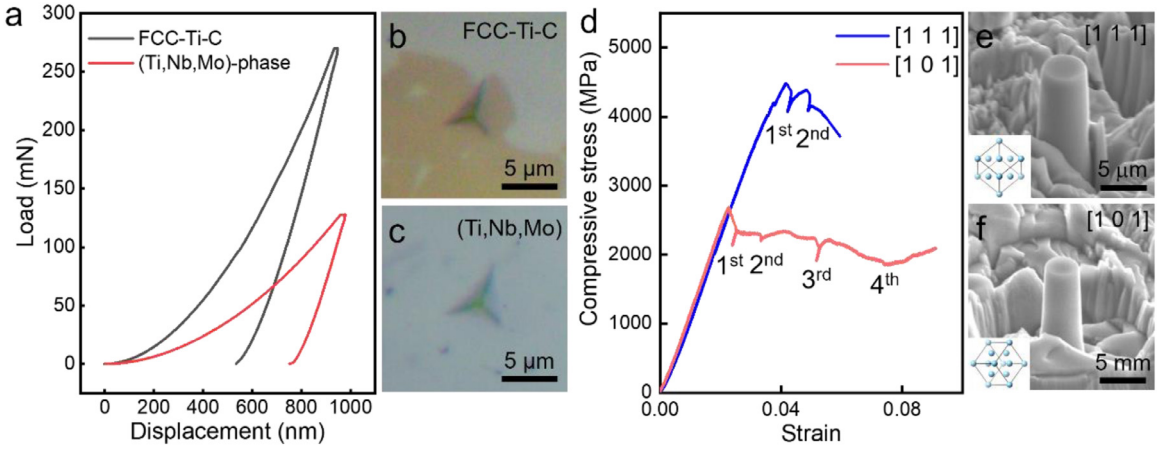

Fig. 4. Mechanical properties of the FCC-Ti-C: a nanoindentation loading-unloading curves of the FCC-Ti-C comparing to the (Ti,Nb,Mo) solid solution phase; b and c corresponding indentation marks on the FCC-Ti-C and (Ti,Nb,Mo) solid solution phase, showing the clear contrast between the two phases under the optical microscope; d compressive stress-strain curves on the FIB-fabricated single-crystal FCC-Ti-C micropillars with different crystallographic orientations; e and f SEM secondary electron images of the as-fabricated single-crystal FCC-Ti-C micropillars.

3.3. Mechanical properties of the FCC-Ti-C

The Young's modulus and nano hardness of the FCC-Ti-C along with the (Ti,Nb,Mo) phase were testing by nanoindentation according to the continuous stiffness method (CSM) and the representative loading-unloading curves are shown in Fig. 4**a**. The nanoindentation results indicated that the FCC-Ti-C possesses much higher Young's modulus (233.1±22.2 GPa) and nano-hardness (17.8±1.9 GPa) than those of the (Ti,Nb,Mo) phase (155.9±3.3 GPa and 6.6±0.2 GPa). Then compression tests were carried out on the FIB fabricated FCC-Ti-C single crystal micropillars to investigate its deformation behavior. For the micropillar compression tests of single-crystal samples, the crystallographic orientation has a significant impact on the deformation behaviors. Here, cylinder samples of the FCC-Ti-C with the [1 0 1] and [1 1 1] direction along the axial direction were chosen as shown in Fig. 4**e** and **f**. The representative engineering stress-strain curves are plotted in Fig. 4**d**. The FCC-Ti-C exhibited ultrahigh compressive strengths (4.48 GPa for the [1 1 1] compression direction and 2.67 GPa for the [1 0 1] compression direction) while relatively poor ductility. By multiplying the Schmit factor [80,81] (0.27 for the [1 1 1] compression direction and 0.41 for the [1 1 0] compression direction), the critical resolved shear stress was calculated to be 1.12±0.07 GPa, which is also remarkably enhanced in comparison with the HCP-Ti [82]. Similar to the compressive strength, the ductility also exhibited an anisotropic characteristic, that the strain to fracture when compressed at [1 0 1] direction was much higher than that of the [1 1 1] direction. As can be seen in Fig. 4**d**, sudden stress drops caused by the dislocation bursts could be observed repeatedly during the compression tests, indicating that planar slipping was the main deformation mechanism. In the case for the FCC-Ti-C compressed along the [1 1 1] crystallographic direction, the dislocation burst occurs at every 0.006 strain, and after two bursts, the micropillar fractured at a total strain of 0.06 before the third burst could happen. As for the FCC-Ti-C compressed along the [1 0 1] crystallographic direction, the first two dislocation bursts also at every 0.006 strain

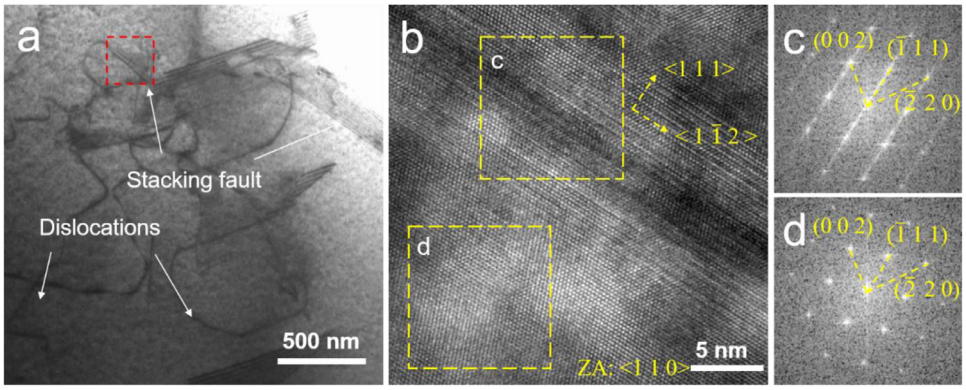

Fig. 5. TEM characterization of deformed FCC-Ti-C: a bright field image; b HRTEM image of the stacking fault in the red dashed square in Figure 5 a; c and d FFT patterns of the marked areas in Figure 5b.

which is similar to that deformed at the [1 1 1] direction, the third and fourth burst took place after every 0.02 strain after the first and second, and led to a much more fracture strain than that of the [1 1 1] direction.

The deformed microstructure of the FCC-Ti-C was characterized by TEM and shown in Fig. 5. As shown in Fig. 5**a**, dislocations and stacking faults can be observed in the deformed FCC-Ti-C sample, indicating that the deformation mechanisms of the FCC-Ti-C are dislocation slipping and stacking fault deformation. The stacking fault was determined to be the typical {1 1 1}<1 1̄ 2> type according to Fig. 5**b-d** which are common in FCC metals such as Co alloys [83]. A serial of two-beam bright-field and dark-field images were taken under different g vectors to determine the type of dislocations and stacking faults (see Fig. S4 and S5 in the supplementary material). The stacking faults were determined to be intrinsic stacking faults using the method proposed by A. Art et al [84]. The dislocations in the FCC-Ti are mainly consist of a/2 <0 1 1>-type perfect dislocations in the {1 1 1}<1 1 0> system and a/6 <1 1 2>-type Shockley partial dislocations together with the stacking faults. As mentioned before, the FCC-Ti contains a high content of interstitial C atoms that could efficiently deteriorate the mobility of dislocations in the FCC lattice, thus the dislocation density was relatively low. As a result, the ductility of the FCC-Ti-C is poorer than that of other allotropic phases of titanium but much better than the titanium carbides [85].

3.4. Ab-initio *studies of the FCC-Ti and the effect of interstitial C atoms*

To understand the nature of this allotropic transformation, *Ab-initio* calculations were carried out. According to the XRD patterns in Fig. 1**a**, it can be deduced that the FCC-Ti was transformed from the BCC phase. Supercells consist of 4 and 16 Ti atoms were created from HCP-Ti, BCC-Ti, and FCC-Ti, and then 1 C atom was doped in the octahedral interstice to construct the Ti-5.8%C and Ti-20%C systems from HCP-Ti, BCC-Ti, and FCC-Ti. As can be seen in Fig. 6, for the BCC-Ti, the cohesive energy raised by 0.13 eV/atom and 0.30 eV/atom as 5.8 at.% and 20 at.% C was doped, indicating that adding C atoms could decrease the stability of the BCC-Ti. For the HCP-Ti and FCC-Ti, however, doping C in the system significantly lowered the cohesive energies which means that C could help stabilize the HCP-Ti and FCC-Ti. What is more, the cohesive energy of HCP-Ti was lower than that of the FCC-Ti which is obvious to all that the HCP-Ti is the stable form of the pure-Ti and C is recognized as a α−stabilizer, but when the C content was increased to a higher level (20 at.% in this case), the cohesive energy of FCC-Ti decreased by a larger amount and became lower than that of the HCP-Ti. The reason behind the difference in energy variation could be attributed to the different symmetry of the atomic arrangement between the FCC and HCP lattices which would lead to differences in interactions between atoms (such as the electrostatic potential energy, the Hartree energy, etc.). As a result, the FCC-Ti with the lowest cohesive energy became the most stable phase when the C content was high and led to the BCC-FCC allotropic transformation of Ti.

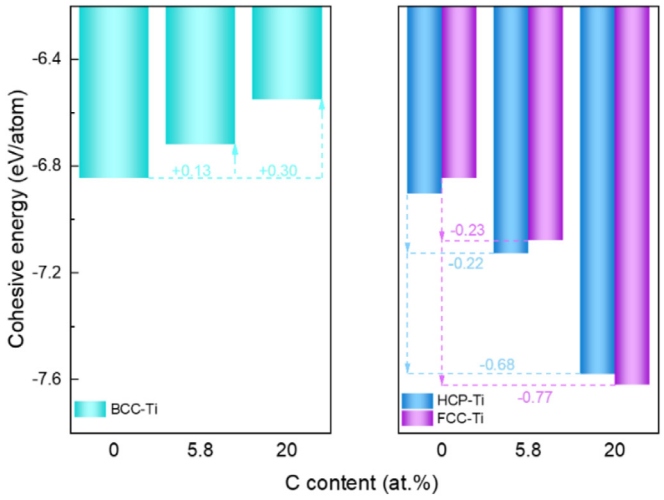

Fig. 6. Cohesive energy variation of BCC-Ti, HCP-Ti, and FCC-Ti caused by different content of interstitial C atoms.

A sea of researches has proven that the generalized stacking fault energy (GSFE) curves to be a useful tool to evaluate the mechanical properties of crystalline materials [86]. The *ab-initio* calculated GSFE curves of the pure FCC-Ti and C-doped FCC-Ti are shown in Fig. 7**a**. the unstable stacking fault energy (γ_{usf}) of the FCC-Ti was calculated to be 115.42 mJ/m^2, the intrinsic stacking fault energy (γ_{isf}) of the FCC-Ti was -214.57 mJ/m^2. In comparison to the traditional HCP-Ti [87], the γ_{usf} which represents the energy barrier of formation of stacking fault is significantly lowered of FCC-Ti, indicating that stacking fault is more likely to form to serve as an alternative deformation mode. As illustrated in the inset of Fig. 7**a**, the intrinsic stacking fault formed an HCP-Ti nucleus (circled in the dashed line), and the negative value of the γ_{isf} suggests that the FCC-Ti would transform into the HCP-Ti once the energy barrier was overcome. After doping one C atom in the octahedral interstice between the 7th and 8th layer of FCC-Ti (1 C-doped FCC-Ti), γ_{usf} increased slightly to 144.43 mJ/m^2 (+28.71 mJ/m^2 with respect to the pure FCC-Ti) and the γ_{isf} increased remarkably to -134.48 mJ/m^2 (+107.09 mJ/m^2 with respect to the

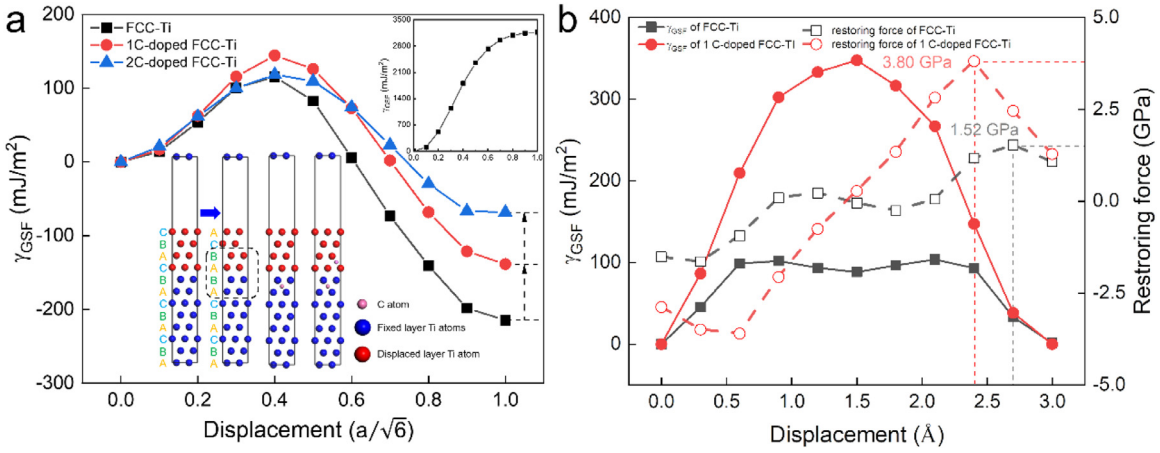

Fig. 7. Mechanical properties of FCC-Ti and C-doped FCC-Ti evaluated by DFT: a {1 1 1}<1 $\bar{1}$ 2> GSFE curves of the pure FCC-Ti, 1C-doped FCC-Ti and 2C-doped FCC-Ti with the insets showing the simulation cells and GSFE curve of the FCC-Ti with one C atom doped in the fault plane; b {1 1 1}<1 $\bar{1}$ 0> system GSFE curves and the restoring force curves of the FCC-Ti and 1 C-doped FCC-Ti.

pure FCC-Ti). When another C atom was doped in the octahedral interstice between the 9th and 10th layer (2 C-doped FCC-Ti), however, γ_{usf} decreased by 25.78 mJ/m^2 to 118.65 mJ/m^2, and the γ_{isf} continued to increase by 66.23 mJ/m^2 to -68.25 mJ/m^2 with respect to the 1 C-doped FCC-Ti. Thus, it can be concluded that interstitial C atoms have little influence on the stacking fault stacking barrier but could significantly raise the energy of the intrinsic stacking fault and tend to prevent the HCP-Ti nuclearization. Another scenario is the C atom is doped between the 8th and 9th layer (at the fault plane), displacement of the upper half of the supercell raised the GSFE dramatically and reach a maximum value at the displacement of a/$\sqrt{6}$ as presented in the upper-right inset of Fig. 7**a**, indicating that the interstitial C atom could strongly hinder the formation of stacking fault on the same plane. The {1 1 1}<1 $\bar{1}$ 0> GSFE curves of FCC-Ti and C-doped FCC-Ti were also calculated as shown in Fig. 7**b**. In comparison to the {1 1 1}<1 $\bar{1}$ 2> system, the γ_{isf} of the {1 1 1}<1 $\bar{1}$ 0> is much higher in an FCC-Ti, and doping C atoms could significantly raise the energy barrier to form an intrinsic stacking fault. As a result, {1 1 1}<1 $\bar{1}$ 2> stacking fault is more preferred to form in the FCC-Ti. The ideal slide stress was also calculated based on the GSFE curves [88] indicating that interstitial C atom could also elevate the ideal slide stress by a large amount to effectively resist the {1 1 1}<1 $\bar{1}$ 0> shear deformation.

The 6×6 elastic tensor of the FCC-Ti with C content ranged from 0 at.% to 33.33 at.% were acquired by structural relaxation and lattice perturbations in the DFT calculations, from which the bulk modulus, shear modulus, isotropic Poisson ratio, and Young's modulus of polycrystalline FCC-Ti were derived as listed in Table S1 in the supplementary materials. According to DFT calculation results, doping C atoms in the octahedral interstices remarkably increased the Young's modulus of the FCC-Ti, from 112 GPa of the pure FCC-Ti to 302 GPa of the 33.3 at.% C-FCC-Ti. The calculated moduli agree well with the tested modulus of the FCC-Ti-C by nanoindentation. The spatial dependence of Young's modulus [89] of the FCC-Ti and FCC-Ti doped with 20% C were presented in the inset of Fig. 8, indicating that the pure FCC-Ti exhibits an anisotropic elastic characteristic, that the single crystal shows the highest modulus at <1 1 1> directions and lowest modulus at <1 0 0> directions. The interstitial C atom significantly altered the anisotropy of the FCC-Ti that the anisotropy index was reduced from 2.223 down to 1.326, and the crystallographic directions that process the highest modulus changed to <1 0 0> directions while the crystallographic directions that process the highest modulus changed to <1 1 1> directions which agreed well with the micropillar compression tests results that the tested Young's modulus at [1 1 1] direction was

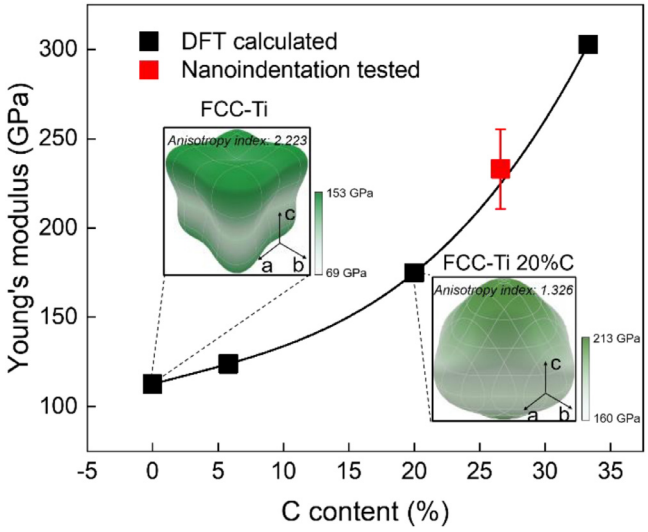

Fig. 8. Calculated Young's moduli of the C-doped FCC-Ti with different C contents based on the DFT calculation results and nanoindentation tested Young's modulus of the FCC-Ti in this work, and the insets are the 3D plot of the spatial dependence of Young's modulus of pure FCC-Ti and 20 at.% C FCC-Ti.

lower than that at [1 0 1] direction and both were much lower than the average modulus tested by nanoindentation according to the CSM.

3.5. Nature of the FCC-Ti phase transformation

The FCC-Ti-C phase was determined to be transformed from a BCC-Ti phase during the hot-press sintering process. Unlike the widely reported HCP to FCC transformations, it is the very first time that the BCC-FCC phase transformation of titanium was investigated. As stated in the published researches, the formation of this novel phase of Ti is due to either energy minimization of thin films or defect (partial dislocation, stacking fault. etc.) movement in the severely deformed bulk Ti alloys. In this case, considering the large size of the FCC-Ti phase, the energy minimization phase transformation mechanism could be instantly ruled out. Although the elemental powder experienced severe deformation during ball milling to achieve mechanical alloying, the following long-duration, high-temperature sintering process which would eliminate the grain defects made it unlikely to be the nature of this transformation. As is

Table 1
Comparative summary of thermal-induced FCC-Ti.

Material	Treatment	Temperature	Impurity (content)	Reference
Ti-15V-3Sn-3Cr-3Al (wt.%)	Aging	600 °C	O (NA)	[42]
Nb-22Ti-16Si-3Al-xCr (wt.%)	TEM heating	850 °C	O (12.3 at.%)	[47]
Ti	TEM heating	700 °C	O (0.05-7.8 at.%)	[50]
Ti-0.1wt.%O	TEM heating	600 °C	O (0.1 wt.%)	[51]
$Ti_{37}Nb_{28}Mo_{28}$-C_7	Hot press sintering	1300 °C	C (26.6 at.%)	This work

known to all, phase transformation occurs towards the lower energy state of the system. According to the cohesive energies of different systems calculated by DFT, the doped interstitial C atoms would raise the cohesive energy of BCC-Ti and make the system less and less stable as the C content increases. As for the HCP-Ti and FCC-Ti, interstitial C atoms would lower the cohesive energies of both the HCP-Ti and FCC-Ti, however, it can be easily concluded based on Fig. 6 that, the HCP-Ti is the stable phase when the C content is low while the FCC-Ti becomes more stable than the HCP-Ti when C content is high. Hence, the doped interstitial C atoms were the key factor of the BCC-FCC allotropic transformation of Ti and could be considered as the "FCC stabilizer of titanium". It is worth mentioning that the GSFE curves of FCC-Ti in Fig. 7 and the reported GSFE curves of HCP-Ti [87,90] also provide indirect evidence of this conclusion, that the interstitial C atoms could raise the γ_{isf} of the FCC-Ti {1 1 1}<1 $\bar{1}$ 2> slip system while lower the γ_{isf} of the HCP-Ti basial slip system (from 306 mJ/m^2 to 269 mJ/m^2 for Ti-O system in reference[87] and from 278.45 mJ/m^2 to 95.89 mJ/m^2 for Ti-C system in reference [90]), indicating that C atoms could impede the HCP-Ti nucleus formation from FCC-Ti while facilitating the FCC-Ti nucleation in the HCP-Ti. In fact, of all the reported thermal-induced FCC-Ti that formed during sintering, annealing, or direct heating, impurity atoms could be detected in the FCC-Ti, as listed in Table 1, yet no attention on their influence was raised [42,47,50,51]. Once the C-induced FCC-Ti was formed, it remained stable at elevated temperatures (as demonstrated by high-temperature annealing and quenching experiment in Supplementary Fig. S6), which is also the case with for the thermal-induced FCC-Ti listed in Table 1. As mentioned in section 3.1, small contents of oxygen were detected in the FCC-Ti-C phase and the BCC (Ti,Nb,Mo)-phase, plus all the FCC-Ti reviewed in Table 1 contain O atoms, it is essential to evaluate the FCC-inducing-abilities of C and O atoms in Ti. Based on the *ab-initio* calculation of the FCC-Ti-O system (shown in Fig. S7 in the supplementary material), the energy variation caused by interstitial O atoms is similar to that caused by C atoms, which means doping O could also induce the BCC-FCC phase transformation. However, unlike carbon, oxygen in the BCC-Ti could lower the system energy, which suggests a good solubility of O in BCC-Ti. The cohesive energy variation from BCC-Ti-X to FCC-Ti-X (X=C or O) was calculated to assess the inducing ability of the BCC-FCC transformation and shown in Fig. S7 **c**. It can be seen that the cohesive energy would decrease by a larger amount from BCC-Ti to FCC-Ti with interstitial C than that with O. Thus, it could be deduced that carbon is the stronger inducing element and the main cause of this BCC-Ti to FCC-Ti transformation. There are possibilities that minor content of O could facilitate the FCC transformation or merely dissolved in the FCC-Ti-C phase after it is formed, more in-depth comparative studies are needed to fully understand the inducing mechanisms of different interstitial elements.

3.6. Strengthening mechanism of the interstitial-C-induced FCC-Ti

Besides being the key factor in inducing the FCC-Ti allotropic transformation, the interstitial C atoms also make a great contribution to the solid solution strengthening effect of the FCC-Ti. The first attempt to test the mechanical properties of FCC-Ti was reported by Yu et al. [51] using in-situ compression on a TEM. Despite using such a nanoscale sample would get a much higher strength due to the size effect, a piece of significant information could be extracted that the compressive strength and Young's modulus of FCC-Ti-O are very similar to that of the HCP-Ti-O of which the CRSS has been reported to be no more than 200 MPa and the Young's modulus of approximately 110 GPa. As mentioned before, the CRSS of the C-induced FCC-Ti was calculated to be 1.12±0.07 GPa, and the Young's modulus was tested to be 233.1±22.2 GPa, which were both considerably elevated compared to the low O content FCC-Ti reported by Yu et al. The ultrahigh strength and modulus were mainly attributed to the high content of interstitial C atoms. On the one hand, the interstitial C atoms could cause lattice distortion and effectively pin the dislocations to provide a solid solution strengthening effect. On the other hand, according to Song et al. [91], the interstitial C atoms in the octahedral sites of Ti lattice would cause a significant raise of charge density around them, and further lead to a remarkable elevation in the modulus and theoretic strength. Comparing to the α-Ti and β-Ti, the FCC-Ti-C in this study exhibited unprecedented high modulus and hardness, which could be a solution to the insufficient stiffness of titanium-based materials in certain applications.

4. Conclusions

In this work, an interstitial-C-induced FCC-Ti formed in a $Ti_{37}Nb_{28}Mo_{28}$-C_7 complex concentrated alloy was discovered and carefully examined. The lattice structure was characterized using Cs-corrected STEM and EELS characterization demonstrated that the C atoms were distributed randomly in the FCC-Ti as solid solute atoms. The mechanical properties of the C-induced FCC-Ti tested by nanoindentation and micropillar compression exhibited that the FCC-Ti-C possesses an extraordinarily high Young's modulus of 233.1 GPa and ultrahigh compressive strengths (4.48 GPa at [1 1 1] direction, 2.67 GPa at [1 0 1] direction and a CRSS of 1.12 ± 0.07 GPa). *Ab-initio* studies revealed that the interstitial C atoms causing the energy variation was the key inducing factor of this FCC allotropic transformation and lead to a reasonable conclusion that thermal-induced FCC-Ti was actually the interstitial-impurity-induced. These findings demonstrated a novel C-induced FCC-Ti with significantly enhanced stiffness and strength which provides new insights into this hidden allotropic phase of Ti and the effect of C atoms on the RCCAs and could widely broaden the possibilities of the property-manipulation of designing Ti-based materials RCCAs.

Author contributions

L.J. H. and S. J. designed the study; S. J. prepared the alloy and specimens and carried out the main experiments; X. G. and S. P. conducted the STEM and EELS characterizations; G. L. helped with the micropillar compression tests; Y. J. helped with the *ab-initio* studies; Q. A., R. Z., and S. W. helped with the data analysis and results interpretation; L. G. offered valuable advice on the orches-

tration of the study. All authors discussed the results and approved the final version of the manuscript.

Declaration of Competing Interest

The authors declare that they have no known competing financial interests or personal relationships that could have appeared to influence the work reported in this paper.

Acknowledgment

This work was financially supported by the National Key R&D Program of China [grant number 2017YFB0703100], Key-Area Research and Development Program of GuangDong Province [grant number 2019B010942001], the National Natural Science Foundation of China [grant numbers 51822103, 51731009 and 51901056], the Fundamental Research Funds for the Central Universities [grant number HIT.BRETIV.201902 and HIT.NSRIF.2020002]. The authors would like to thank Mr. Shaolou Wei for the suggestions on *ab-initio* studies and Prof. Jianbo Wang from Wuhan University for providing the Cs-corrected STEM characterization platform. The authors also would like to send their blessings to celebrate the 100th anniversary of Harbin Institute of Technology.

Supplementary materials

Supplementary material associated with this article can be found, in the online version, at doi:10.1016/j.actamat.2020.10.075.

References

[1] G. He, J. Eckert, W. Loser, L. Schultz, Novel Ti-base nanostructure-dendrite composite with enhanced plasticity, Nature materials 2 (1) (2003) 33–37.
[2] Y. Chang, W. Lu, J. Guenole, L.T. Stephenson, A. Szczpaniak, P. Kontis, A.K. Ackerman, F.F. Dear, I. Mouton, X. Zhong, S. Zhang, D. Dye, C.H. Liebscher, D. Ponge, S. Korte-Kerzel, D. Raabe, B. Gault, Ti and its alloys as examples of cryogenic focused ion beam milling of environmentally-sensitive materials, Nature Communication 10 (1) (2019) 942.
[3] L.J. Huang, L. Geng, H-X Peng, Microstructurally inhomogeneous composites: is a homogeneous reinforcement distribution optimal? Progress in Materials Science 71 (2015) 93–168.
[4] T.M. Pollock, Alloy design for aircraft engines, Nature Materials 15 (2016) 809.
[5] G. Singh, U. Ramamurty, Boron modified titanium alloys, Progress in Materials Science 111 (2020) 100653.
[6] D. Banerjee, J.C. Williams, Perspectives on Titanium Science and Technology, Acta Materialia 61 (3) (2013) 844–879.
[7] H. Huang, Y. Wu, J. He, H. Wang, X. Liu, K. An, W. Wu, Z. Lu, Phase-Transformation Ductilization of Brittle High-Entropy Alloys via Metastability Engineering, Advanced Materials 29 (30) (2017) 1701678.
[8] S. Wei, S.J. Kim, J. Kang, Y. Zhang, Y. Zhang, T. Furuhara, E.S. Park, C.C. Tasan, Natural-mixing guided design of refractory high-entropy alloys with as-cast tensile ductility, Nature Materials (2020).
[9] Z. Lei, X. Liu, Y. Wu, H. Wang, S. Jiang, S. Wang, X. Hui, Y. Wu, B. Gault, P. Kontis, D. Raabe, L. Gu, Q. Zhang, H. Chen, H. Wang, J. Liu, K. An, Q. Zeng, T.-G. Nieh, Z. Lu, Enhanced strength and ductility in a high-entropy alloy via ordered oxygen complexes, Nature 563 (7732) (2018) 546–550.
[10] S. Maiti, W. Steurer, Structural-disorder and its effect on mechanical properties in single-phase TaNbHfZr high-entropy alloy, Acta Materialia 106 (2016) 87–97.
[11] S. Zherebtsov, N. Yurchenko, E. Panina, M. Tikhonovsky, N. Stepanov, Gum-like mechanical behavior of a partially ordered Al5Nb24Ti40V5Zr26 high entropy alloy, Intermetallics 116 (2020) 106652.
[12] D. Shaysultanov, A. Nepapushev, S. Zherebtsov, D. Moskovskikh, N. Stepanov, Structure and mechanical properties of a low-density AlCrFeTi medium entropy alloy produced by spark plasma sintering, Materials Science and Engineering: A 795 (2020) 140018.
[13] L. Wang, C. Fu, Y. Wu, R. Li, X. Hui, Y. Wang, Superelastic effect in Ti-rich high entropy alloys via stress-induced martensitic transformation, Scripta Materialia 162 (2019) 112–117.
[14] L. Lilensten, J.-P. Couzinié, J. Bourgon, L. Perrière, G. Dirras, F. Prima, I. Guillot, Design and tensile properties of a bcc Ti-rich high-entropy alloy with transformation-induced plasticity, Materials Research Letters 5 (2) (2017) 110–116.
[15] O.N. Senkov, D.B. Miracle, K.J. Chaput, J.-P. Couzinie, Development and exploration of refractory high entropy alloys—A review, Journal of materials research 33 (19) (2018) 3092–3128.
[16] Z. Li, C.C. Tasan, H. Springer, B. Gault, D. Raabe, Interstitial atoms enable joint twinning and transformation induced plasticity in strong and ductile high-entropy alloys, Scientific Reports 7 (1) (2017) 40704.
[17] Z. Li, D. Raabe, Strong and Ductile Non-equiatomic High-Entropy Alloys: Design, Processing, Microstructure, and Mechanical Properties, JOM 69 (11) (2017) 2099–2106.
[18] J.B. Seol, J.W. Bae, Z. Li, J. Chan Han, J.G. Kim, D. Raabe, H.S. Kim, Boron doped ultrastrong and ductile high-entropy alloys, Acta Materialia 151 (2018) 366–376.
[19] M. Wang, Z. Li, D. Raabe, In-situ SEM observation of phase transformation and twinning mechanisms in an interstitial high-entropy alloy, Acta Materialia 147 (2018) 236–246.
[20] Y. Chen, Y. Li, X. Cheng, Z. Xu, C. Wu, B. Cheng, M. Wang, Interstitial strengthening of refractory ZrTiHfNb0.5Ta0.5Ox (x = 0.05, 0.1, 0.2) high-entropy alloys, Materials Letters 228 (2018) 145–147.
[21] L.J. Huang, L. Geng, A.B. Li, G.S. Wang, X.P. Cui, Effects of hot compression and heat treatment on the microstructure and tensile property of Ti–6.5Al–3.5Mo–1.5Zr–0.3Si alloy, Materials Science and Engineering: A 489 (1) (2008) 330–336.
[22] X. Ma, F. Li, X. Fang, Z. Li, Z. Sun, J. Hou, J. Cao, Effect of strain reversal on the stress-induced martensitic transformation and tensile properties of a metastable β titanium alloy, Journal of Alloys and Compounds 784 (2019) 111–116.
[23] J. Zhang, C.C. Tasan, M.J. Lai, A.C. Dippel, D. Raabe, Complexion-mediated martensitic phase transformation in Titanium, Nature Communications 8 (2017) 14210.
[24] M. Wang, Y. Lu, B. Pang, Z.T. Kloenne, H.L. Fraser, Y.L. Chiu, M.H. Loretto, Fine alpha in current and newly developed Ti alloys, Acta Materialia 173 (2019) 242–248.
[25] K. Chou, E.A. Marquis, Oxygen effects on ω and α phase transformations in a metastable β Ti–Nb alloy, Acta Materialia 181 (2019) 367–376.
[26] S. Balachandran, A. Kashiwar, A. Choudhury, D. Banerjee, R. Shi, Y. Wang, On variant distribution and coarsening behavior of the α phase in a metastable β titanium alloy, Acta Materialia 106 (2016) 374–387.
[27] S. Balachandran, S. Kumar, D. Banerjee, On recrystallization of the α and β phases in titanium alloys, Acta Materialia 131 (2017) 423–434.
[28] F.E. Wawner, K.R. Lawless, Epitaxial Growth of Titanium Thin Films, Journal of Vacuum Science Technology 6 (4) (1969) 588–590.
[29] D.V. Heerden, D. Josell, D. Shechtman, The formation of f.c.c. titanium in titanium-aluminum multilayers, Acta Materialia 44 (1) (1996) 297–306.
[30] A.F. Jankowski, M.A. Wall, Formation of face-centered cubic titanium on a Ni single crystal and in Ni/Ti multilayers, Journal of Materials Research 9 (1) (1994) 31–38.
[31] J. Kong, H. Shen, B. Chen, Z. Li, W. Shi, W. Yao, Z. Qi, The abnormal structure of nanocrystalline titanium films prepared by d.c. sputtering, Thin Solid Films 207 (1) (1992) 51–53.
[32] Y. Yamada, K. Yoshida, Growth and structure of titanium evaporated films, Applied Surface Science 33-34 (1988) 465–471.
[33] J. Chakraborty, K. Kumar, R. Ranjan, S.G. Chowdhury, S.R. Singh, Thickness-dependent fcc–hcp phase transformation in polycrystalline titanium thin films, Acta Materialia 59 (7) (2011) 2615–2623.
[34] A.A. Saleh, V. Shutthanandan, N.R. Shivaparan, R.J. Smith, T.T. Tran, S.A. Chambers, Epitaxial growth of fcc Ti films on Al(001) surfaces, Physical Review B 56 (15) (1997) 9841–9847.
[35] R. Banerjee, S.A. Dregia, H.L. Fraser, Stability of f.c.c. titanium in titanium/aluminum multilayers, Acta Materialia 47 (15) (1999) 4225–4231.
[36] C.G. Rhodes, N.E. Paton, Formation characteristics of the α/β interface phase in Ti-6Ai-4v, Metallurgical Transactions A 10 (2) (1979) 209.
[37] C. Rhodes, N.J.M.T.A. Paton, The influence of α/β interface phase on tensile properties of Ti-6Al-4V, 10(11) (1979) 1753-1758.
[38] C.G. Rhodes, J.C. Williams, Observations of an interface phase in the α/β boundaries in titanium alloys, Metallurgical Transactions A 6 (8) (1975) 1670.
[39] C.G. Rhodes, J.C. Williams, The precipitation of α-phase in metastable β-phase Ti alloys, Metallurgical Transactions A 6 (11) (1975) 2103–2114.
[40] I. Manna, P.P. Chattopadhyay, P. Nandi, F. Banhart, H.J. Fecht, Formation of face–centered-cubic titanium by mechanical attrition, Journal of Applied Physics 93 (3) (2003) 1520–1524.
[41] D.L. Zhang, D.Y. Ying, Formation of fcc titanium during heating high energy ball milled Al–Ti powders, Materials Letters 52 (4–5) (2002) 329–333.
[42] R. Sarkar, P. Ghosal, K.S. Prasad, T.K. Nandy, K.K. Ray, An FCC phase in a metastable β-titanium alloy, Philosophical Magazine Letters 94 (5) (2014) 311–318.
[43] H.C. Wu, A. Kumar, J. Wang, X.F. Bi, C.N. Tome, Z. Zhang, S.X. Mao, Rolling-induced Face Centered Cubic Titanium in Hexagonal Close Packed Titanium at Room Temperature, Scientific Reports 6 (2016) 24370.
[44] C. Chen, S. Qian, S. Wang, L. Niu, R. Liu, B. Liao, Z. Zhong, P. Lu, P. Li, L. Cao, The microstructure and formation mechanism of face-centered cubic Ti in commercial pure Ti foils during tensile deformation at room temperature, Materials Characterization 136 (2017) 257–263.
[45] S. Wang, L. Niu, C. Chen, Y. Pang, B. Liao, Z.H. Zhong, P. Lu, P. Li, X.D. Wu, J.W. Coenen, L.F. Cao, Y.C. Wu, Size effects on the tensile properties and deformation mechanism of commercial pure titanium foils, Materials Science and Engineering: A 730 (2018) 244–261.
[46] B. Wei, S. Ni, Y. Liu, M. Song, Three dimensional crystallographic orientation relationships for hexagonal close packed structure to face centered cubic structure transformation in pure titanium, Scripta Materialia 169 (2019) 46–51.
[47] X. Ma, X. Guo, M. Fu, Y. Qiao, In-situ TEM observation of hcp-Ti to fcc-Ti phase transformation in Nb-Ti-Si based alloys, Materials Characterization 142 (2018) 332–339.

[48] G. Han, X. Lu, Q. Xia, B. Lei, Y. Yan, C.J. Shang, Face-centered-cubic titanium - A new crystal structure of Ti in a Ti-8Mo-6Fe alloy, Journal of Alloys and Compounds 748 (2018) 943–952.
[49] R. Jing, C.Y. Liu, M.Z. Ma, R.P. Liu, Microstructural evolution and formation mechanism of FCC titanium during heat treatment processing, Journal of Alloys and Compounds 552 (2013) 202–207.
[50] R. Traylor, R. Zhang, J. Kacher, J.O. Douglas, P.A.J. Bagot, A.M. Minor, Impurity and texture driven HCP-to-FCC transformations in Ti-X thin films during in situ TEM annealing and FIB milling, Acta Materialia 184 (2020) 199–210.
[51] Q. Yu, J. Kacher, C. Gammer, R. Traylor, A. Samanta, Z. Yang, A.M. Minor, In situ TEM observation of FCC Ti formation at elevated temperatures, Scripta Materialia 140 (2017) 9–12.
[52] S. Xiong, W. Qi, B. Huang, M. Wang, Z. Li, S. Liang, Size–Temperature Phase Diagram of Titanium Nanosolids, The Journal of Physical Chemistry C 116 (1) (2011) 237–241.
[53] Z.P. Chen, Z. Wen, Q. Jiang, Phase stabilities of fcc Ti nanocrystals, Solid State Communications 132 (11) (2004) 747–750.
[54] L.P. Yue, W.G. Yao, Z.Z. Qi, Y.Z. He, Structure of nanometer-size crystalline Ti film, Nanostructured Materials 4 (4) (1994) 451–456.
[55] D. Banerjee, V.S. Arunachalam, On the $\alpha\beta$ interface phase in Ti alloys, Acta Metallurgica 29 (10) (1981) 1685–1694.
[56] D. Banerjee, Identification of the Interface Phase in Titanium Alloys, Metallurgical Transactions A 13 (4) (1982) 681–684.
[57] D. Banerjee, J.C. Williams, The effect of foil preparation technique on interface phase formation in Ti alloys, Scripta Metallurgica 17 (9) (1983) 1125–1128.
[58] D. Banerjee, C.G. Shelton, B. Ralph, J.C. Williams, A resolution of the interface phase problem in titanium alloys, Acta Metallurgica 36 (1) (1988) 125–141.
[59] Y. Chang, S. Zhang, C.H. Liebscher, D. Dye, D. Ponge, C. Scheu, G. Dehm, D. Raabe, B. Gault, W. Lu, Could face-centered cubic titanium in cold-rolled commercially-pure titanium only be a Ti-hydride? Scripta Materialia 178 (2020) 39–43.
[60] D. Banerjee, Comments on 'Composite structure of α phase in metastable β Ti alloys induced by lattice strain during β to α phase transformation', Scripta Materialia 141 (2017) 146–147.
[61] M. de Jong, W. Chen, T. Angsten, A. Jain, R. Notestine, A. Gamst, M. Sluiter, C. Krishna Ande, S. van der Zwaag, J.J. Plata, C. Toher, S. Curtarolo, G. Ceder, K.A. Persson, M. Asta, Charting the complete elastic properties of inorganic crystalline compounds, Scientific Data 2 (2015) 150009.
[62] D.H. Chung, W.R. Buessem, The Voigt-Reuss-Hill Approximation and Elastic Moduli of Polycrystalline MgO, CaF2, β-ZnS, ZnSe, and CdTe, Journal of Applied Physics 38 (6) (1967) 2535–2540.
[63] H.J. Seifert, H.L. Lukas, G. Petzow, Thermodynamic optimization of the Ti-C system, Journal of Phase Equilibria 17 (1) (1996) 24–35.
[64] X.-F. Gu, T. Furuhara, W.-Z. Zhang, PTCLab: free and open-source software for calculating phase transformation crystallography, Journal of applied crystallography 49 (3) (2016) 1099–1106.
[65] G. Kurdjumov, G. Sachs, Oberden mechanismus det stahlhirtung, Z. Physik 64 (1930) 225.
[66] S. Wei, L. Huang, X. Li, Q. An, L. Geng, Interactive effects of cyclic oxidation and structural evolution for Ti-6Al-4V/(TiC+ TiB) alloy composites at elevated temperatures, Journal of Alloys and Compounds 752 (2018) 164–178.
[67] P.D. Nellist, The Principles of STEM Imaging, in: S.J. Pennycook, P.D. Nellist (Eds.), Scanning Transmission Electron Microscopy: Imaging and Analysis, Springer New York, New York, NY, 2011, pp. 91–115.
[68] S. Jiang, H. Wang, Y. Wu, X. Liu, H. Chen, M. Yao, B. Gault, D. Ponge, D. Raabe, A. Hirata, M. Chen, Y. Wang, Z. Lu, Ultrastrong steel via minimal lattice misfit and high-density nanoprecipitation, Nature 544 (7651) (2017) 460–464.
[69] W. Sun, Y. Zhu, R. Marceau, L. Wang, Q. Zhang, X. Gao, C. Hutchinson, Precipitation strengthening of aluminum alloys by room-temperature cyclic plasticity, Science 363 (6430) (2019) 972–975.
[70] J. Lee, W. Zhou, S.J. Pennycook, J.-C. Idrobo, S.T. Pantelides, Direct visualization of reversible dynamics in a Si6 cluster embedded in a graphene pore, Nature Communications 4 (2013) 1650.
[71] X. Gao, C.A.J. Fisher, T. Kimura, Y.H. Ikuhara, H. Moriwake, A. Kuwabara, H. Oki, T. Tojigamori, R. Huang, Y. Ikuhara, Lithium Atom and A-Site Vacancy Distributions in Lanthanum Lithium Titanate, Chemistry of Materials 25 (9) (2013) 1607–1614.
[72] S.D. Findlay, N. Shibata, H. Sawada, E. Okunishi, Y. Kondo, T. Yamamoto, Y. Ikuhara, Robust atomic resolution imaging of light elements using scanning transmission electron microscopy, Applied Physics Letters 95 (19) (2009) 191913.
[73] X. Gao, Y.H. Ikuhara, C.A.J. Fisher, H. Moriwake, A. Kuwabara, H. Oki, K. Kohama, R. Yoshida, R. Huang, Y. Ikuhara, Structural Distortion and Compositional Gradients Adjacent to Epitaxial LiMn2O4 Thin Film Interfaces, Advanced Materials Interfaces 1 (8) (2014) 1400143.
[74] S. Wei, L. Huang, Y. Zhu, Z. Shi, X. Li, L. Geng, Sub-stoichiometry-facilitated oxidation kinetics in a δ-TixC-doped Ti-based alloy, npj Materials Degradation 3 (1) (2019) 3.
[75] J. Buršík, G. Weatherly, Ordering of Substoichiometric δ-TiCx Phase in Ti–V–C Alloys, physica status solidi 174(2) (1999) 327-335.
[76] F. Hofer, F.P. Schmidt, W. Grogger, G. Kothleitner, Fundamentals of electron energy-loss spectroscopy, IOP Conference Series: Materials Science and Engineering 109 (2016) 012007.
[77] R.D. Leapman, L.A. Grunes, P.L. Fejes, Study of the L_{23} edges in the $3d$ transition metals and their oxides by electron-energy-loss spectroscopy with comparisons to theory, Physical Review B 26 (2) (1982) 614–635.
[78] H. Daniels, R. Brydson, B. Rand, A. Brown, Investigating carbonization and graphitization using electron energy loss spectroscopy (EELS) in the transmission electron microscope (TEM), Philosophical Magazine 87 (27) (2007) 4073–4092.
[79] K. Chen, S. Kamran, Bonding characteristics of tic and tin, Modeling Numerical Simulation of Material Science 3 (1) (2013) 7.
[80] A. Cruzado, B. Gan, M. Jiménez, D. Barba, K. Ostolaza, A. Linaza, J.M. Molina-Aldareguia, J. Llorca, J. Segurado, Multiscale modeling of the mechanical behavior of IN718 superalloy based on micropillar compression and computational homogenization, Acta Materialia 98 (2015) 242–253.
[81] E. Paccou, B. Tanguy, M. Legros, Micropillar compression study of Fe-irradiated 304L steel, Scripta Materialia 172 (2019) 56–60.
[82] T.-S. Jun, Z. Zhang, G. Sernicola, F.P.E. Dunne, T.B. Britton, Local strain rate sensitivity of single α phase within a dual-phase Ti alloy, Acta Materialia 107 (2016) 298–309.
[83] T.L. Achmad, W. Fu, H. Chen, C. Zhang, Z.-G. Yang, First-principles calculations of generalized-stacking-fault-energy of Co-based alloys, Computational Materials Science 121 (2016) 86–96.
[84] A. Art, R. Gevers, S. Amelinckx, The Determination of the Type of Stacking Faults in Face Centered Cubic Alloys by Means of Contrast Effects in the Electron Microscope, 3(4) (1963) 697-711.
[85] I. El Azhari, J. Garcia, M. Zamanzade, F. Soldera, C. Pauly, L. Llanes, F. Mücklich, Investigations on micro-mechanical properties of polycrystalline Ti(C,N) and Zr(C,N) coatings, Acta Materialia 149 (2018) 364–376.
[86] C. Kale, P. Garg, B.G. Bazehhour, S. Srinivasan, M.A. Bhatia, P. Peralta, K.N. Solanki, Oxygen effects on crystal plasticity of Titanium: A multiscale calibration and validation framework, Acta Materialia 176 (2019) 19–32.
[87] P. Kwasniak, H. Garbacz, K.J. Kurzydlowski, Solid solution strengthening of hexagonal titanium alloys: Restoring forces and stacking faults calculated from first principles, Acta Materialia 102 (2016) 304–314.
[88] S.H. Zhang, D. Legut, R.F. Zhang, PNADIS: An automated Peierls–Nabarro analyzer for dislocation core structure and slip resistance, Computer Physics Communications 240 (2019) 60–73.
[89] R. Gaillac, P. Pullumbi, F.-X. Coudert, ELATE: an open-source online application for analysis and visualization of elastic tensors, Journal of Physics: Condensed Matter 28 (27) (2016) 275201.
[90] P. Garg, M.A. Bhatia, K.N. Solanki, Uncovering the influence of metallic and non-metallic impurities on the ideal shear strength and ductility of Ti: An ab–initio study, Journal of Alloys and Compounds 788 (2019) 413–421.
[91] Y. Song, Z.X. Guo, R. Yang, Influence of interstitial elements on the bulk modulus and theoretical strength of a-titanium: A first-principles study, Philosophical Magazine A 82 (7) (2002) 1345–1359.